

# A basic Michelson laser interferometer for the undergraduate teaching laboratory demonstrating picometer sensitivity

Kenneth G. Libbrecht<sup>a)</sup> and Eric D. Black<sup>b)</sup>  
264-33 Caltech, Pasadena, California 91125

(Received 3 July 2014; accepted 4 November 2014)

We describe a basic Michelson laser interferometer experiment for the undergraduate teaching laboratory that achieves picometer sensitivity in a hands-on, table-top instrument. In addition to providing an introduction to interferometer physics and optical hardware, the experiment also focuses on precision measurement techniques including servo control, signal modulation, phase-sensitive detection, and different types of signal averaging. Students examine these techniques in a series of steps that take them from micron-scale sensitivity using direct fringe counting to picometer sensitivity using a modulated signal and phase-sensitive signal averaging. After students assemble, align, and characterize the interferometer, they then use it to measure nanoscale motions of a simple harmonic oscillator system as a substantive example of how laser interferometry can be used as an effective tool in experimental science. © 2015 American Association of Physics Teachers. [<http://dx.doi.org/10.1119/1.4901972>]

## I. INTRODUCTION

Optical interferometry is a well-known experimental technique for making precision displacement measurements, with examples ranging from Michelson and Morley's famous aether-drift experiment to the extraordinary sensitivity of modern gravitational-wave detectors. By carefully managing a variety of fundamental and technical noise sources, displacement sensitivities of better than  $10^{-19}$  m/Hz<sup>-1/2</sup> have been demonstrated (roughly  $10^{-13}$  wavelengths of light).<sup>1,2</sup>

Given the widespread use of interferometric measurement techniques in experimental science, we sought to construct a fairly basic, yet high-precision, Michelson interferometer for use in our undergraduate teaching laboratory. Students in the course would likely have no previous background in optics or interferometry, and our goals for this project included four needs. First, we wanted to produce a compact instrument that gives students hands-on experience with optical and laser hardware, including optical alignment. Second, we wanted to use a minimal optical layout to reduce complexity and cost. Third, we wanted to provide a brief but nontrivial introduction to modern measurement techniques, including servo control, signal modulation, phase-sensitive detection, and different types of signal averaging. Fourth, we wanted to demonstrate the highest displacement sensitivity that is practically achievable without enshrouding the instrument beneath layers of acoustic and seismic isolation.

A literature search quickly revealed an enormous selection of potentially relevant references describing the multitude of uses of laser interferometry for a broad range of measurements. Given our goals, however, we soon turned our attention away from many papers describing low-sensitivity interferometry, including the basic fringe-counting Michelson interferometers that have been used for many years in teaching labs to measure, for example, the indices of refraction of gases or thermal expansion coefficients.<sup>3-7</sup>

One also encounters numerous examples in the literature of laser interferometers demonstrating picometer sensitivity using instruments of greater complexity than the basic Michelson, requiring some combination of additional optical elements, more elaborate optical layouts, frequency-modulated lasers, frequency-shifting acousto-optical modulators, homodyne or

heterodyne readouts, and perhaps multiple lasers.<sup>8-14</sup> Modern interferometry review articles tend to focus on complex optical configurations as well,<sup>15</sup> as they offer improved sensitivity and stability over simpler designs. While these advanced instrument strategies are becoming the norm in research and industry, for educational purposes we sought to develop a basic Michelson interferometer that uses the archetypal optical layout often found in textbooks, and we found that these advanced techniques were not compatible with our objectives.

We soon narrowed our literature search to precision displacement measurements using basic (single-beam) Michelson interferometers.<sup>16-18</sup> Precision interferometry is certainly not a new subject, and these references describe interferometers that are similar to the one we describe below. During the building phase of our project, however, we soon found that many experimental details not provided in our references were quite critical for achieving picometer sensitivity. These include the choice of optical components and mounting hardware, optical alignment specifics, unwanted mechanical resonances, servo design, managing seismic and acoustic noise, and devising suitable measurement strategies. We generally found that these specifics were difficult to find in the literature, being dispersed over many sources if they could be found at all. In an attempt to remedy this situation, we describe below the construction and characterization of a basic Michelson interferometer in some detail, and we focus as well on its use in the instructional laboratory.

Our final instrument is designed for physics teaching. It is visual and tactile, relatively easy to understand, and generally fun to work with, making it well suited for training students. It demonstrates precision physical measurement techniques in a compact apparatus with a simple optical layout. Students place some of the optical components themselves and then align the interferometer, thus gaining hands-on experience with optical and laser hardware. The alignment is straightforward but not trivial, and the various interferometer signals are directly observable on the oscilloscope. Some features of the instrument include:<sup>16-18</sup> (1) piezoelectric control of one mirror's position, allowing precise control of the interferometer signal, (2) the ability to lock the interferometer at its most sensitive point, (3) the ability to modulate the mirror position while the interferometer is

locked, thus providing a displacement signal of variable magnitude and frequency, and (4) phase-sensitive detection of the modulated displacement signal, both using the digital oscilloscope and using basic analog signal processing.

In working with this experiment, students are guided through a series of measurement strategies, from micron-scale measurement precision using direct fringe counting to picometer precision using a modulated signal and phase-sensitive signal averaging. The end result is the ability to see displacement modulations below one picometer in a 10-cm-long interferometer arm, which is like measuring the distance from New York to Los Angeles with a sensitivity better than the width of a human hair.

Once the interferometer performance has been explored, students then incorporate a magnetically driven oscillating mirror in the optical layout.<sup>21</sup> Observation and analysis of nanometer-scale motions of the high- $Q$  oscillator reveal several aspects of its behavior, including: (1) the near-resonant-frequency response of the oscillator, (2) mass-dependent frequency shifts, (3) changes in the mechanical  $Q$  as damping is added, and (4) the excitation of the oscillator via higher harmonics using a square-wave drive signal.

With this apparatus, students learn about optical hardware and lasers, optical alignment, laser interferometry, piezoelectric transducers, photodetection, electronic signal processing, signal modulation to avoid low-frequency noise, signal averaging, and phase-sensitive detection. Achieving a displacement sensitivity of 1/100th of an atom with a table-top instrument provides an impressive demonstration of the power of interferometric measurement and signal-averaging techniques. Further quantifying the behavior of a mechanical oscillator executing nanoscale motions shows the effectiveness of laser interferometry as a measurement tool in experimental science.

## II. INTERFEROMETER DESIGN AND PERFORMANCE

Figure 1 shows the overall optical layout of the constructed interferometer. The 12.7-mm-thick aluminum breadboard (Thorlabs MB1224) is mounted atop a custom-made steel electronics chassis using rubber vibration dampers, and the chassis itself rests on rubber feet. The rubber dampers are all approximately 25 mm in size (length and diameter) with 50 A durometer. We found that this two-stage seismic

isolation system is adequate for reducing noise in the interferometer signal arising from benchtop vibrations, as long as the benchtop is not bumped or otherwise unnecessarily perturbed. This is particularly true for the phase-sensitive measurements described below, which are done at sufficiently high frequencies that only modest damping of seismic noise is needed.

The helium-neon laser (Meredith HNS-2P) produces a 2 mW linearly polarized (500:1 polarization ratio) 633-nm beam with a diameter of approximately 0.8 mm, and it is mounted in a pair of custom fixed acrylic holders. The beamsplitter (Thorlabs BSW10) is a 1-in.-diameter wedged plate beamsplitter with a broadband dielectric coating giving roughly equal transmitted and reflected beams. It is mounted in a fixed optical mount (Thorlabs FMP1) connected to a pedestal post (Thorlabs RS1.5P8E) fastened to the breadboard using a clamping fork (Thorlabs CF125). Mirrors 1 and 2 (both Thorlabs BB1-E02) are mounted in standard optical mounts (Thorlabs KM100) on the same pedestal posts. Using these stout steel pedestal posts is important for reducing unwanted motions of the optical elements.

We note that while inexpensive diode lasers are often adequate for making simple fringe-counting interferometers, in general they are not well suited for precision interferometry. In our experience, diode lasers have poor beam shapes, can exhibit large frequency jumps, often run multi-mode, and are sensitive to back reflection. As a result, the fringe quality of a diode-laser interferometer is often erratic. In contrast, 633-nm helium-neon lasers typically show a nearly ideal Gaussian mode shape, good frequency stability, and a much smaller optical bandwidth.

The mirror/PZT consists of a small mirror (12.5-mm diameter, 2-mm thick, Edmund Optics 83-483, with an enhanced aluminum reflective coating) glued to one end of a piezoelectric stack transducer (PZT) (Steminc SMPAK155510D10), with the other end glued to an acrylic disk in a mirror mount. An acrylic tube surrounds the mirror/PZT assembly for protection, but the mirror only contacts the PZT stack. The surface quality of the small mirror is relatively poor (2–3 waves over one cm) compared with the other mirrors, but we found it is adequate for this task, and the small mass of the mirror helps push mechanical resonances of the mirror/PZT assembly to frequencies above 700 Hz.

The photodetector includes a Si photodiode (Thorlabs FDS100) with a 3.6 mm  $\times$  3.6 mm active area, held in a

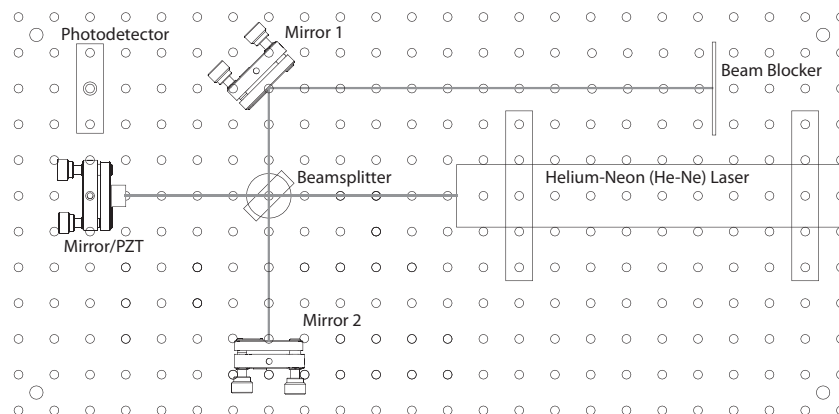


Fig. 1. The interferometer optical layout on an aluminum breadboard with mounting holes on a 25.4-mm grid. The mirror/PZT consists of a small mirror glued to a piezoelectric stack mounted to a standard optical mirror mount. Mirrors 1 and 2 are basic steering mirrors, and the beamsplitter is a wedge with a 50:50 dielectric coating.

custom acrylic fixed mount. The custom photodiode amplifier consists of a pair of operational amplifiers (TL072) that provide double-pole low-pass filtering of the photodiode signal with a  $10\text{-}\mu\text{s}$  time constant, as shown in Fig. 4. The overall amplifier gain is fixed, giving approximately an 8-V output signal with the full laser intensity incident on the photodiode's active area.

The optical layout shown in Fig. 1 was designed to provide enough degrees of freedom to fully align the interferometer, but no more. The mirror/PZT pointing determines the degree to which the beam is misaligned from retroreflecting back into the laser (described below), the mirror 2 pointing allows for alignment of the recombining beams, and the mirror 1 pointing is used to center the beam on the photodiode. In addition to reducing the cost of the interferometer and its maintenance, using a small number of optical elements also reduces the complexity of the set-up, improving its function as a teaching tool.

Three of the optical elements (mirror 1, mirror 2, and the beamsplitter) can be repositioned on the breadboard or removed. The other three elements (the laser, photodiode, and the mirror/PZT) are fixed on the breadboard, the only available adjustment being the pointing of the mirror/PZT. The latter three elements all need electrical connections, and for these the wiring is sent down through existing holes in the breadboard and into the electronics chassis below. The use of fixed wiring (with essentially no accessible cabling) allows for an especially compact and robust construction that simplifies the operation and maintenance of the interferometer. At the same time, the three free elements present students with a realistic experience placing and aligning laser optics.

Before setting up the interferometer as in Fig. 1, there are a number of smaller exercises students can do with this instrument. The Gaussian laser beam profile can be observed, as well as the divergence of the laser beam. Using a concave lens (Thorlabs LD1464-A,  $f = -50\text{ mm}$ ) increases the beam divergence and allows a better look at the beam profile. Laser speckle can also be observed, as well as diffraction from small bits of dirt on the optics. Ghost laser beams from the antireflection-coated side of the beamsplitter are clearly visible, as the wedge in the glass sends these beams out at different directions from the main beams. Rotating the beamsplitter  $180^\circ$  results in a different set of ghost beams, and it is instructive to explain these with a sketch of the two reflecting surfaces and the resulting intensities of multiply reflected beams.

### A. Interferometer alignment

A satisfactory alignment of the interferometer is straightforward and easy to achieve, but doing so requires an understanding of how real-world optics can differ from the idealized case that is often presented. As shown in Fig. 2, retroreflecting the laser beams at the ends of the interferometer arms yields a recombined beam that is sent directly back toward the laser. This beam typically reflects off the front mirror of the laser and reenters the interferometer, yielding an optical cacophony of multiple reflections and unwanted interference effects. Inserting an optical isolator in the original laser beam would solve this problem, but this is an especially expensive optical element that is best avoided in the teaching lab.

The preferred solution to this problem is to misalign the arm mirrors slightly, as shown in Fig. 2. With our

components and the optical layout shown in Fig. 1, misaligning the mirror/PZT by  $4.3\text{ mrad}$  is sufficient that the initial reflection from the mirror/PZT avoids striking the front mirror of the laser altogether, thus eliminating unwanted reflections. This misalignment puts a constraint on the lengths of the two arms, however, as can be seen from the second diagram in Fig. 2. If the two arm lengths are identical (as in the diagram), then identical misalignments of both arm mirrors can yield (in principle) perfectly recombined beams that are overlapping and collinear beyond the beamsplitter. If the arm lengths are not identical, however, then perfect recombination is no longer possible.

The arm length asymmetry constraint can be quantified by measuring the fringe contrast seen by the detector. If the position  $x$  of the mirror/PZT is varied over small distances, then the detector voltage can be written

$$V_{\text{det}} = V_{\text{min}} + \frac{1}{2}(V_{\text{max}} - V_{\text{min}})[1 + \cos(2kx)], \quad (1)$$

where  $V_{\text{min}}$  and  $V_{\text{max}}$  are the minimum and maximum voltages, respectively, and  $k = 2\pi/\lambda$  is the wavenumber of the laser. This signal is easily observed by sending a triangle wave to the PZT, thus translating the mirror back and forth, while  $V_{\text{det}}$  is observed on the oscilloscope. We define the interferometer fringe contrast to be

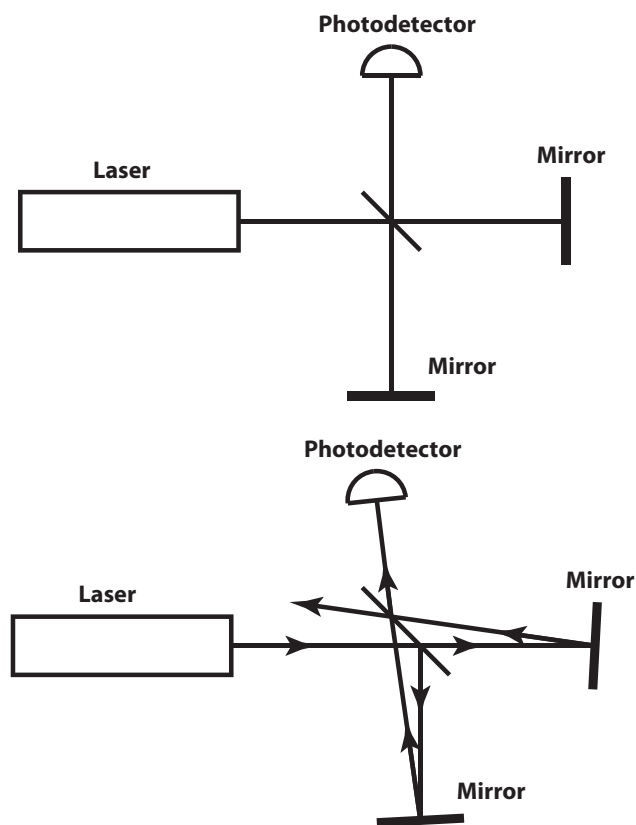


Fig. 2. Although the top diagram is often used to depict a basic Michelson interferometer, in reality this configuration is impractical. Reflections from the front mirror of the laser produce multiple interfering interferometers that greatly complicate the signal seen at the photodetector. In contrast, the lower diagram shows how a slight misalignment (exaggerated in the diagram) eliminates these unwanted reflections without the need for additional optical elements. In the misaligned case, however, complete overlap of the recombined beams is only possible if the arm lengths of the interferometer are equal.

$$F_C = \frac{V_{\max} - V_{\min}}{V_{\max} + V_{\min}}, \quad (2)$$

and a high fringe contrast with  $F_C \approx 1$  is desirable for obtaining the best interferometer sensitivity.

With this background, the interferometer alignment consists of the following steps. (1) Place the beamsplitter so the reflected beam is at a  $90^\circ$  angle from the original laser beam. The beamsplitter coating is designed for a  $90^\circ$  reflection angle, plus it is generally good practice to keep the beams on a simple rectangular grid as much as possible. (2) With mirror 2 blocked, adjust the mirror/PZT pointing so the reflected beam just misses the front mirror of the laser. This is easily done by observing any multiple reflections at the photodiode using a white card. (3) Adjust the mirror 1 pointing so the beam is centered on the photodiode. (4) Unblock mirror 2 and adjust its pointing to produce a single recombined beam at the photodiode. (5) Send a triangle wave signal to the PZT, observe  $V_{\text{det}}$  with the oscilloscope, and adjust the mirror 2 pointing further to obtain a maximum fringe contrast  $F_{C,\max}$ .

Figure 3 shows our measurements of  $F_{C,\max}$  as a function of the mirror 2 arm length when the mirror/PZT misalignment was set to 4.3 mrad and the mirror/PZT arm length was 110 mm. As expected, the highest  $F_{C,\max}$  was achieved when the arm lengths were equal. With unequal arm lengths, perfect recombination of the beams is not possible, and we see that  $F_{C,\max}$  drops off quadratically with an increasing asymmetry in the arm lengths.

As another alignment test, we misaligned the mirror/PZT by 1.3 mrad and otherwise followed the same alignment procedure described above, giving the other set of data points shown in Fig. 3. With this smaller misalignment, there were multiple unwanted reflections from the front mirror of the laser, but these extra beams were displaced just enough to miss the active area of the photodetector. In this case, we see a weaker quadratic dependence of  $F_{C,\max}$  on the mirror 2 position, and about the same  $F_{C,\max}$  when the arm lengths are identical.

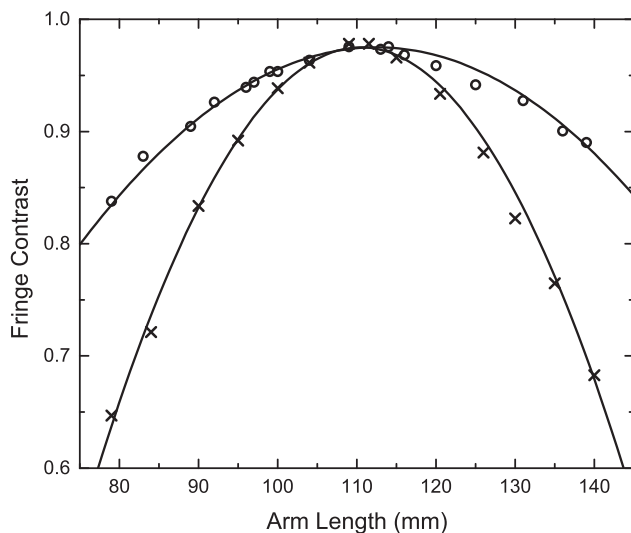


Fig. 3. The measured fringe contrast  $F_{C,\max}$  as a function of the length of the mirror 2 arm of the interferometer. For each data point, mirror 2 was repositioned and reclamped, and then the mirror 2 pointing was adjusted to obtain the maximum possible fringe contrast. The  $\times$  data points were taken with a mirror/PZT misalignment of 4.3 mrad (relative to retroreflection), while the circles were taken with a misalignment of 1.3 mrad. The lines show parabolic fits to the data.

We did not examine why  $F_{C,\max}$  is below unity for identical arm lengths, but this is likely caused by the beamsplitter producing unequal beam intensities, and perhaps by other optical imperfections in our system. The peak value of about 97% shows little dependence on polarization angle, as observed by rotating the laser tube in its mount. Extrapolating the data in Fig. 3 to zero misalignment suggests that the laser has an intrinsic coherence length of roughly 15 cm. We did not investigate the origin of this coherence length, although it appears likely that it arises in part from the excitation of more than one longitudinal mode in the laser cavity.

The smaller 1.3-mrad misalignment produces a higher fringe contrast for unequal arm lengths, but this also requires that students deal with what can be a confusing array of unwanted reflections. When setting up the interferometer configuration shown in Fig. 1, we typically have students use the larger misalignment of 4.3 mrad, which is set up by observing and then quickly eliminating the unwanted reflections off the front mirror of the laser. We then ask students to match the interferometer arm lengths to an accuracy of a few millimeters, as this can be done quite easily from direct visual measurement using a plastic ruler.

Once the interferometer is roughly aligned (with the 4.3 mrad misalignment), it is also instructive to view the optical fringes by eye using a white card. Placing a negative lens in front of the beamsplitter yields a bull's-eye pattern of fringes at the photodetector, and this pattern changes as the mirror 2 pointing is adjusted. Placing the same lens after the beamsplitter gives a linear pattern of fringes, and the imperfect best fringe contrast can be easily seen by attempting (unsuccessfully) to produce a perfectly dark fringe on the card.

## B. Interferometer locking

The interferometer is locked using the electronic servo circuit shown in Fig. 4. In short, the photodiode signal  $V_{\text{det}}$  is fed back to the PZT via this circuit to keep the signal at some constant average value, thus keeping the arm length difference constant to typically much better than  $\lambda/2$ . The total range of the PZT is only about  $1 \mu\text{m}$  (with an applied voltage ranging from 0 to 24 V), but this is sufficient to keep the interferometer locked for hours at a time provided the system is stable and undisturbed. Typically, the set point is adjusted so the interferometer is locked at  $V_{\text{det}} = (V_{\min} + V_{\max})/2$ , which is the point where the interferometer sensitivity  $dV_{\text{det}}/dx$  is highest.

Note that the detector signal  $V_{\text{det}}$  is easily calibrated by measuring  $\Delta V = V_{\max} - V_{\min}$  on the oscilloscope and using Eq. (1), giving the conveniently simple approximation

$$\left(\frac{dV_{\text{det}}}{dx}\right)_{\max} \approx \frac{\Delta V}{100 \text{ nm}}, \quad (3)$$

which is accurate to better than one percent (but only for a 633-nm helium-neon laser). Simultaneously measuring  $V_{\text{det}}$  and the voltage  $V_{\text{PZT}}$  sent to the PZT via the Scan IN port (see Fig. 4) quickly gives the absolute PZT response function  $dx/dV_{\text{PZT}}$ .

The PZT can also be modulated with the servo locked using the circuit in Fig. 4 along with an external modulation signal. Figure 5 shows the interferometer response as a function of modulation frequency in this case, for a fixed input modulation signal amplitude. To produce these data, we

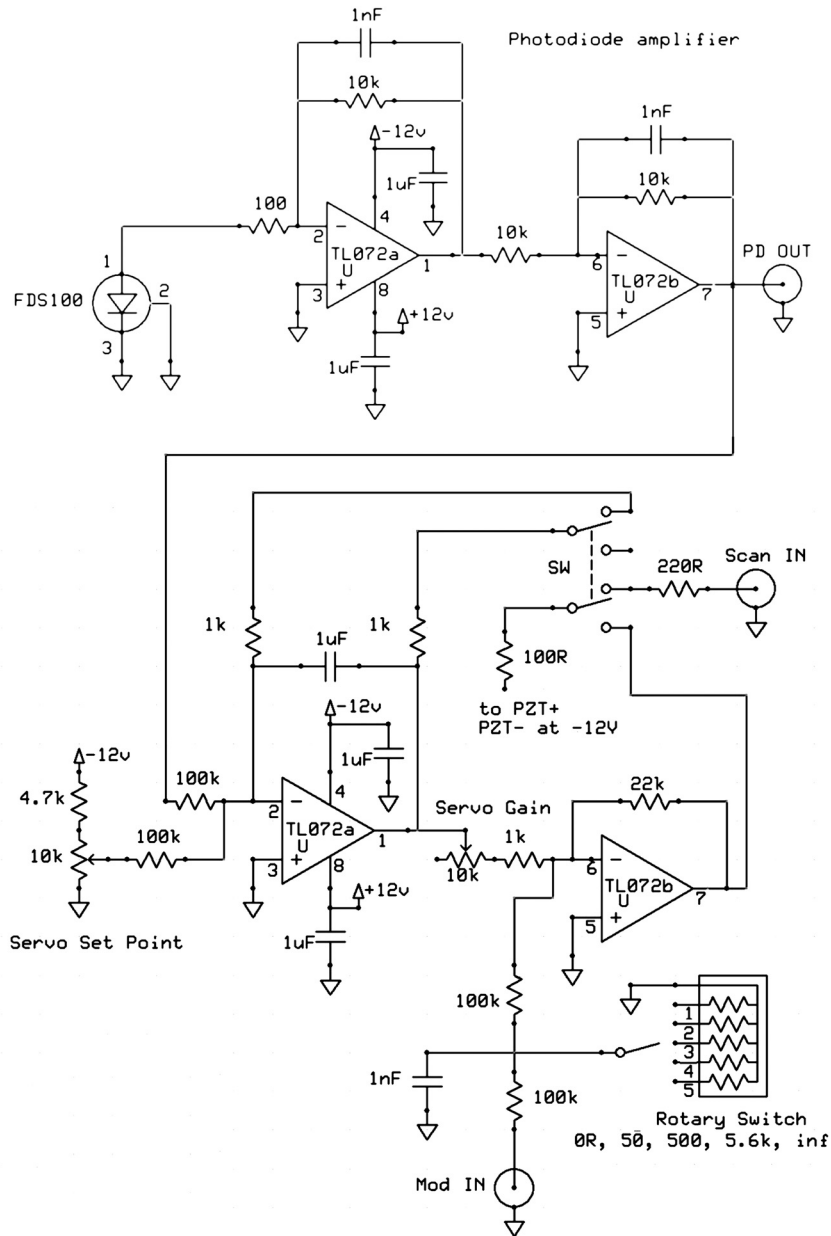


Fig. 4. The electronics used to scan, lock, and modulate the interferometer signal. With switch SW in the SCAN position, a signal input to the Scan IN port is sent essentially directly to the PZT. With the switch in the LOCK position, a feedback loop locks the mirror/PZT so the average photodiode signal (PD Out) equals the Servo Set Point. With the interferometer locked, a signal sent to the Mod IN port additionally modulates the mirror position. A resistor divider is used to turn off the modulation or reduce its amplitude by a factor of 1, 10, 100, or 1000.

locked the interferometer at  $V_{\text{det}} = (V_{\text{min}} + V_{\text{max}})/2$  and provided a constant-amplitude sine-wave signal to the modulation input port shown in Fig. 4. The resulting sine-wave response of  $V_{\text{det}}$  was then measured using a digital oscilloscope for different values of the modulation frequency, with the servo gain at its minimum and maximum settings (see Fig. 4).

A straightforward analysis of the servo circuit predicts that the interferometer response should be given by

$$|\delta V_{\text{det}}| = AG_1 V_{\text{mod}} \left[ 1 + \frac{AG_2}{2\pi\tau\nu} \right]^{-1/2}, \quad (4)$$

where  $A(\nu) = dV_{\text{det}}/dV_{\text{PZT}}$  includes the frequency-dependent PZT response,  $\nu$  is the modulation frequency,  $V_{\text{mod}}$  is the modulation voltage, and the remaining

parameters ( $G_1 = 0.11$ ;  $G_2 = 22$  (high gain), 2 (low gain);  $\tau = RC = 0.1$  s) can be derived from the servo circuit elements shown in Fig. 4. Direct measurements yielded  $A(\nu) \approx 3.15$ , where this number was nearly frequency-independent below 600 Hz and dropped off substantially above 1 kHz. In addition, a number of mechanical resonances in the mirror/PZT housing were also seen above 700 Hz. The theory curves shown in Fig. 5 assume a frequency-independent  $A(\nu)$  for simplicity.

From these data, we see that at low frequencies the servo compensates for the modulation input, reducing the interferometer response, and the reduction is larger when the servo gain is higher. This behavior is well described by the servo circuit theory. At frequencies above about 700 Hz, the data begin to deviate substantially from the simple theory. The theory curves in principle contain no adjustable parameters,

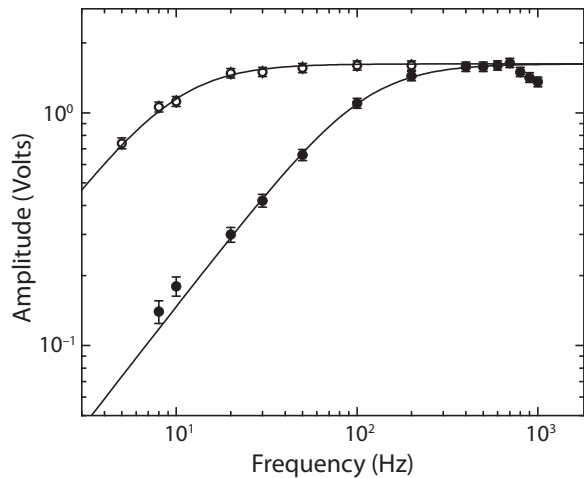


Fig. 5. Measurements of the interferometer response as a function of the PZT modulation frequency, with the servo locked. The upper and lower data points were obtained with the servo gain at its lowest and highest settings, respectively, using the servo control circuit shown in Fig. 4. The theory curves were derived from an analysis of the servo control circuit, using parameters that were measured or derived from circuit elements. To better match the data, the two theory curves each include an additional multiplicative factor of 0.94, consistent with the estimated overall uncertainty in determining the circuit parameters.

but we found that the data were better matched by including an overall multiplicative factor of 0.94 in the theory. This six-percent discrepancy was consistent with the overall uncertainties in the various circuit parameters.

### C. Phase-sensitive detection

Since the purpose of building an interferometer is typically to measure small displacement signals, we sought to produce the highest displacement sensitivity we could easily build in a compact teaching instrument. With the interferometer locked at its most sensitive point, direct observations of fluctuations in  $V_{\text{det}}$  indicate an ambient displacement noise of roughly 1 nm RMS over short timescales at the maximum servo gain, and about 4 nm at the minimum servo gain. Long-term drifts are compensated for by the servo, and these drifts were not investigated further. The short-term noise is mainly caused by local seismic and acoustic noise. Tapping on the table or talking around the interferometer clearly increases these noise sources.

To quantify the interferometer sensitivity, we modulated the PZT with a square wave signal at various amplitudes and frequencies, and we observed the resulting changes in  $V_{\text{det}}$ . The environmental noise sources were greater at lower frequencies (typical of  $1/f$  noise), so we found it optimal to modulate the PZT at around 600 Hz. This frequency was

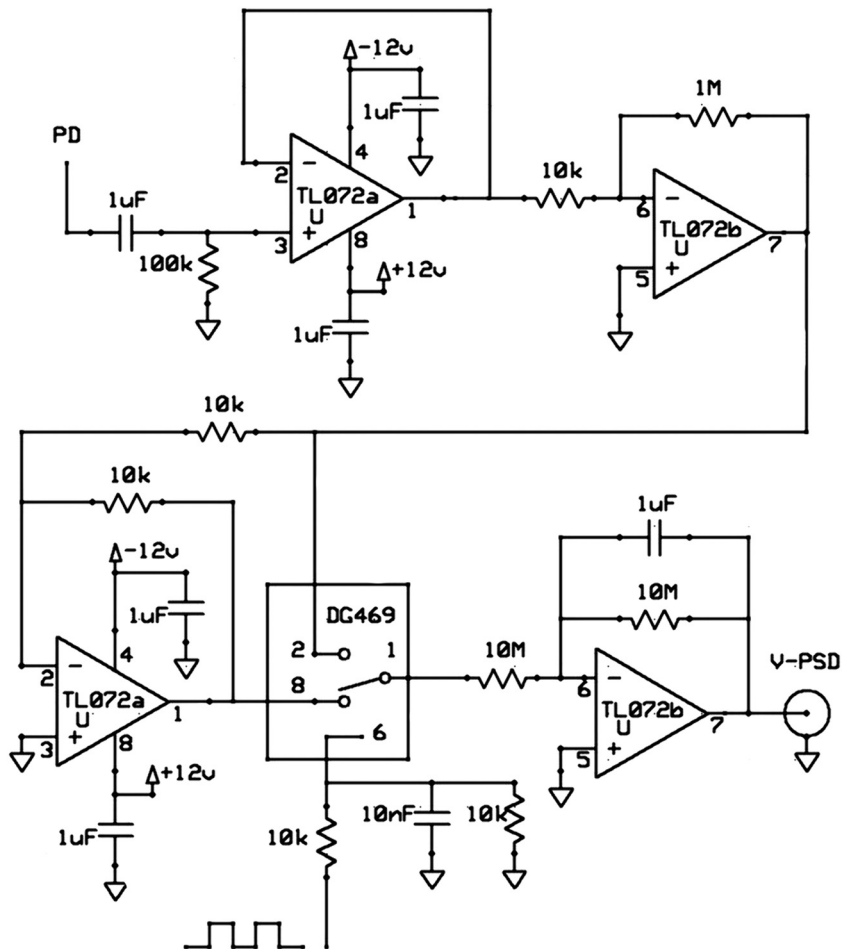


Fig. 6. The electronics used to perform a phase-sensitive detection and averaging of the modulated interferometer signal. The input signal from the photodiode amplifier (PD) is first low-pass filtered and further amplified, plus a negative copy is produced with a  $G = -1$  amplifier. An analog electronic switch chops between these two signals, driven synchronously with the modulation input, and the result is amplified and averaged using a low-pass filter with a time constant of 10 s.

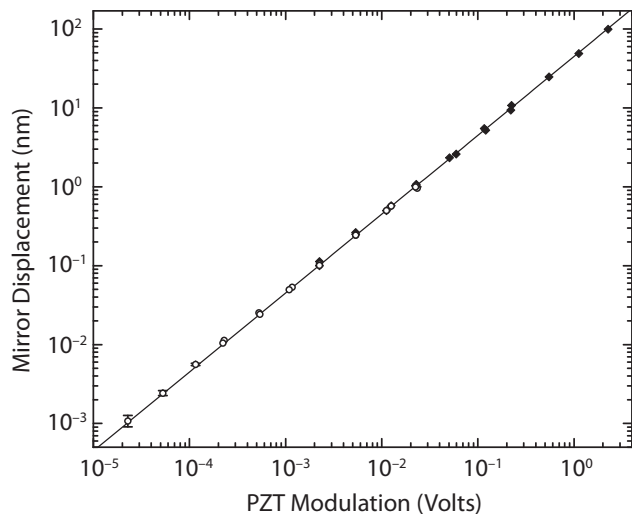


Fig. 7. The measured mirror displacement when the piezoelectric transducer was driven with a square wave modulation at 600 Hz, as a function of the modulation amplitude. The high-amplitude points (closed diamonds) were measured by observing the photodiode signal directly on the oscilloscope, while the low-amplitude points (open circles) were measured using the phase-sensitive averaging circuit shown in Fig. 6. The fit line gives a PZT response of 45 nm/V. These data indicate that the combined PZT and photodiode responses are quite linear over a range of five orders of magnitude in amplitude. At the lowest modulation amplitudes, the noise in the averaged interferometer signal was below one picometer for 10-s averaging times.

above much of the environmental noise and above where the signal was reduced by the servo, but below the mechanical resonances in the PZT housing.

With a large modulation amplitude, one can observe and measure the response in  $V_{\text{det}}$  directly on the oscilloscope, as the signal/noise ratio is high for a single modulation cycle. At lower amplitudes, the signal is better observed by averaging traces using the digital oscilloscope, while triggering with the synchronous modulation input signal. By averaging 128 traces, for example, one can see signals that are about ten times lower than is possible without averaging, as expected.

To carry this process further, we constructed the basic phase-sensitive detector circuit shown in Fig. 6, which is essentially a simple (and inexpensive) alternative to using a lock-in amplifier.<sup>19,20</sup> By integrating for ten seconds, this circuit averages the modulation signal over about 6000 cycles,

thus providing nearly another order-of-magnitude improvement over signal averaging using the oscilloscope. The output  $V_{\text{PSD}}$  from this averaging circuit also provides a convenient voltage proportional to the interferometer modulation signal that can be used for additional data analysis. For example, observing the distribution of fluctuations in  $V_{\text{PSD}}$  over timescales of minutes to hours gives a measure of the uncertainty in the displacement measurement being made by the interferometer.

Our pedagogical goal in including these measurement strategies is to introduce students to some of the fundamentals of modern signal analysis. Observing the interferometer signal directly on the oscilloscope is the most basic measurement technique, but it is also the least sensitive, as the direct signal is strongly affected by environmental noise. A substantial first improvement is obtained by modulating the signal at higher frequencies, thus avoiding the low-frequency noise components. Simple signal averaging using the digital oscilloscope further increases the signal/noise ratio, demonstrating a simple form of phase-sensitive detection and averaging, using the strong modulation input signal to trigger the oscilloscope. Additional averaging using the circuit in Fig. 4 yields an expected additional improvement in sensitivity. Seeing the gains in sensitivity at each stage in the experiment introduces students to the concepts of signal modulation, phase-sensitive detection, and signal averaging, driving home the  $\sqrt{N}$  averaging rule.

#### D. Interferometer response

Figure 7 shows the measured interferometer response at 600 Hz as a function of the PZT modulation amplitude. When the displacement amplitude was above 0.1 nm, the modulation signal was strong enough to be measured using the digital oscilloscope's measure feature while averaging traces. At low displacement amplitudes, the signal became essentially unmeasurable using the oscilloscope alone, but still appeared with high signal-to-noise using the  $V_{\text{PSD}}$  output. The overlap between these two methods was used to determine a scaling factor between them. The absolute measurement accuracy was about 5% for these data, while the  $1\sigma$  displacement sensitivity at the lowest amplitudes was below 1 picometer. These data indicate that systematic nonlinearities in the photodiode and the PZT stack response were together below 10% over a range of five orders of magnitude.

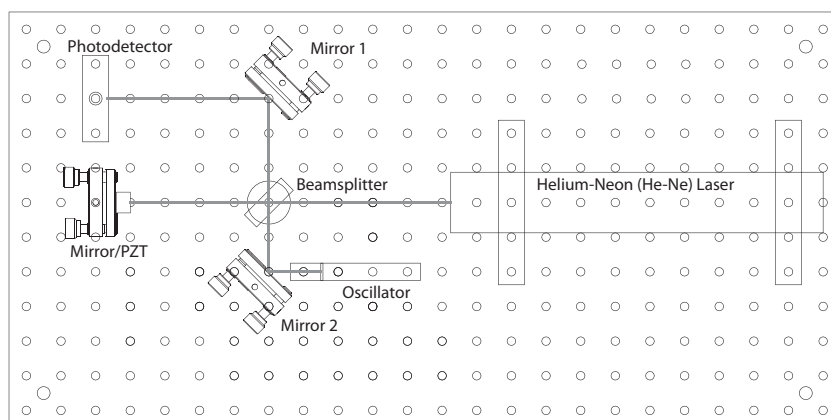


Fig. 8. The interferometer optical layout including the mechanical oscillator shown in detail in Fig. 9.

### III. MEASURING A SIMPLE HARMONIC OSCILLATOR

Once students have constructed, aligned, and characterized the interferometer, they can then use it to observe the nanoscale motions of a simple harmonic oscillator.<sup>21</sup> The optical layout for this second stage of the experiment is shown in Fig. 8, and the mechanical construction of the oscillator is shown in Fig. 9. Wiring for the coil runs through a vertical hole in the aluminum plate (below the coil but not shown in Fig. 9) and then through one of the holes in the breadboard to the electronics chassis below. For this reason the oscillator position on the breadboard cannot be changed, but it does not interfere with the basic interferometer layout shown in Fig. 1.

The oscillator response can be observed by viewing the interferometer signal together with the coil drive signal on the oscilloscope, and example data are shown in Fig. 10. Here, the coil was driven with a sinusoidal signal from a digital function generator with  $<1$  mHz absolute frequency accuracy, and the oscillator response was measured for each point by averaging 64 traces on the oscilloscope. Once again, using the drive signal to trigger the oscilloscope ensures a good phase-locked average even with a small signal amplitude. As shown also in Fig. 7, sub-nanometer sensitivity is easily achievable using this simple signal-averaging method. The results in Fig. 10 show that this mechanical system is well described by a simple-harmonic-oscillator model. Inserting a small piece of foam between the magnet and the coil substantially increases the oscillator damping, and students can examine this by measuring the oscillator  $Q$  with different amounts of damping.

The tapped mounting hole behind the oscillator mirror (see Fig. 9) allows additional weights to be added to the oscillator. We use nylon, aluminium, steel, and brass thumb-screws and nuts to give a series of weights with roughly equal mass spacings. Students weigh the masses using an inexpensive digital scale with 0.1-g accuracy (American

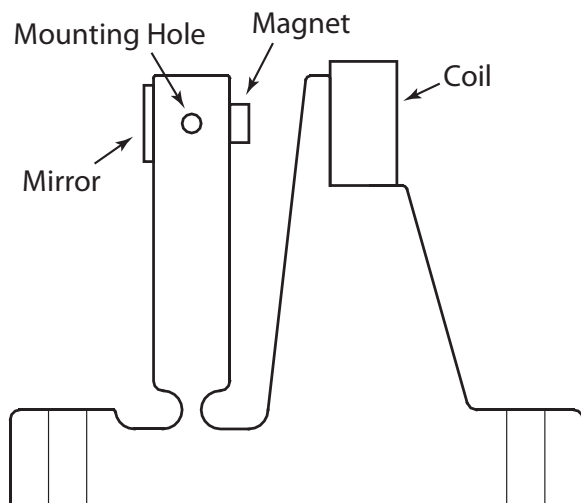


Fig. 9. A side view of the magnetically driven mechanical oscillator shown in Fig. 8. The main body is constructed from 12.7-mm-thick aluminum plate (alloy 6061), and the two vertical holes in the base are 76.2 mm apart to match the holes in the breadboard. Sending an alternating current through the coil applies a corresponding force to the permanent magnet, driving torsional oscillations of the mirror arm about its narrow pivot point. Additional weights can be added to the 8-32 tapped mounting hole to change the resonance frequency of the oscillator.

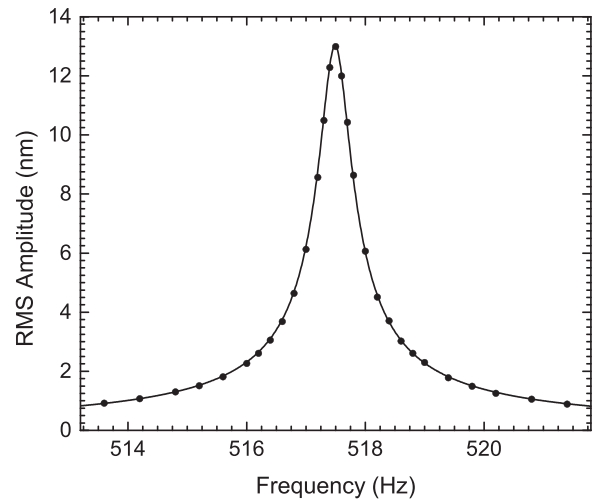


Fig. 10. The measured response of the oscillator as a function of drive frequency. The absolute root-mean-square (RMS) amplitude was derived optically from the interferometer signal. The response is well matched by a simple-harmonic-oscillator model (fit line), indicating a mechanical  $Q$  of 970.

Weigh AWS-100). To achieve satisfactory results, we have found that the weights need to be well balanced (with one on each side of the oscillator), screwed in firmly, and no more than about 1.5 cm in total length. If these conditions are not met, additional mechanical resonances can influence the oscillator response.

The resonance frequency  $\nu_0$  of the oscillator can be satisfactorily measured by finding the maximum oscillator amplitude as a function of frequency, viewing the signal directly on the oscilloscope, and an accuracy of better than 1 Hz can be obtained quite quickly with a simple analog signal generator using the oscilloscope to measure the drive frequency. The results shown in Fig. 11 show that  $\nu_0^{-2}$  is proportional to the added mass, which is expected from a simple-harmonic-oscillator model. Additional parameters describing the harmonic oscillator characteristics can be extracted from the slope and intercept of the fit line.

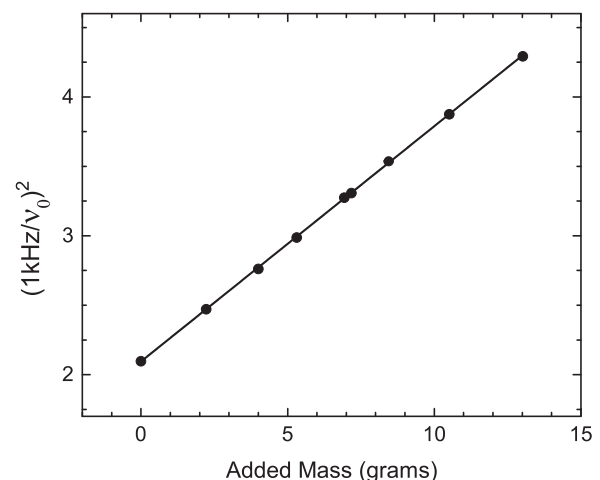


Fig. 11. Measured changes in the resonance frequency  $\nu_0$  of the oscillator as a function of the mass added to the mounting hole shown in Fig. 9. Simple-harmonic-oscillator theory predicts that  $\nu_0^{-2}$  should scale linearly with added mass. The spring constant and moment of inertia of the oscillator can be extracted from the slope and intercept of the fit line.

As a final experiment, students can drive the coil with a square wave signal at different frequencies to observe the resulting motion. The oscillator shows a resonant behavior when the coil is driven at  $\nu_0$ ,  $\nu_0/3$ ,  $\nu_0/5$ , etc., and at each of these frequencies the oscillator response remains at  $\nu_0$ . Measurements of the peak resonance amplitude at each frequency show the behavior expected from a Fourier decomposition of the square-wave signal.

In summary, we have developed a fairly basic table-top precision laser interferometer for use in the undergraduate teaching laboratory. Students first assemble and align the interferometer, gaining hands-on experience using optical and laser hardware. The experiment then focuses on a variety of measurement strategies and signal-averaging techniques, with the goal of using the interferometer to demonstrate picometer displacement sensitivity over arm lengths of 10 centimeters. In a second stage of the experiment, students use the interferometer to quantify the nanoscale motions of a driven harmonic oscillator system.

A sample student lab manual is available as an online supplement to this article.<sup>22</sup> Information about a commercial version of this interferometer can be found at Newtonian Labs.<sup>23</sup>

## ACKNOWLEDGMENTS

This work was supported in part by the California Institute of Technology and by a generous donation from Dr. Vineer Bhansali. Frank Rice contributed insightful ideas to several aspects of the interferometer construction and data analysis.

<sup>a</sup>)Electronic mail: kgl@caltech.edu

<sup>b</sup>)Electronic mail: blacke@its.caltech.edu

<sup>1</sup>K. Riles, "Gravitational waves: Sources, detection, and searches," e-print [arXiv:1209.0667](https://arxiv.org/abs/1209.0667).

<sup>2</sup>E. D. Black, A. Villar, and K. G. Libbrecht, "Thermoelastic-damping noise from sapphire mirrors in a fundamental-noise-limited interferometer," *Phys. Rev. Lett.* **93**, 241101-1-4 (2004).

<sup>3</sup>J. H. Blatt, P. Pollard, and S. Sandilan, "Simple automatic fringe counter for interferometric measurement of index of refraction of gases," *Am. J. Phys.* **42**, 1029-1030 (1974).

<sup>4</sup>M. A. Jeppesen, "Measurement of dispersion of gases with a Michelson interferometer," *Am. J. Phys.* **35**, 435-437 (1967).

<sup>5</sup>J. J. Fendley, "Measurement of refractive index using a Michelson interferometer," *Phys. Educ.* **17**, 209-211 (1982).

<sup>6</sup>R. Scholl and B. W. Liby, "Using a Michelson interferometer to measure coefficient of thermal expansion of copper," *Phys. Teach.* **47**, 306-308 (2009).

<sup>7</sup>G. Dacosta, G. Kiedansky, and R. Siri, "Optoelectronic seismograph using a Michelson interferometer with a sliding mirror," *Am. J. Phys.* **56**, 993-997 (1988).

<sup>8</sup>J. Lawall and E. Kessler, "Michelson interferometry with 10 pm accuracy," *Rev. Sci. Instrum.* **71**, 2669-2676 (2000).

<sup>9</sup>C. Chao, Z. Wang, and W. Zhu, "Modulated laser interferometer with picometer resolution for piezoelectric characterization," *Rev. Sci. Instrum.* **75**, 4641-4645 (2004).

<sup>10</sup>M. Pisani, "A homodyne Michelson interferometer with sub-picometer resolution," *Meas. Sci. Technol.* **20**, 084008-1-6 (2009).

<sup>11</sup>P. Kochert *et al.*, "Phase measurement of various commercial heterodyne He-Ne-laser interferometers with stability in the picometer regime," *Meas. Sci. Technol.* **23**, 074005-1-6 (2012).

<sup>12</sup>W. Denk and W. W. Webb, "Optical measurement of picometer displacements of transparent microscopic objects," *Appl. Opt.* **29**, 2382-2391 (1990).

<sup>13</sup>S. H. Yim, D. Cho, and J. Park, "Two-frequency interferometer for a displacement measurement," *Am. J. Phys.* **81**, 153-159 (2013).

<sup>14</sup>R. H. Belansky and K. H. Wanser, "Laser Doppler velocimetry using a bulk optic Michelson interferometer: A student laboratory experiment," *Am. J. Phys.* **61**, 1014-1019 (1993).

<sup>15</sup>N. Bobroff, "Recent advances in displacement measuring interferometry," *Meas. Sci. Technol.* **4**, 907-926 (1993).

<sup>16</sup>J. F. Li, P. Moses, and D. Viehland, "Simple, high-resolution interferometer for the measurement of frequency-dependent complex piezoelectric responses in ferroelectric ceramics," *Rev. Sci. Instrum.* **66**, 215-221 (1995).

<sup>17</sup>R. Yimmirun, P. J. Moses, R. J. Meyer *et al.*, "A single-beam interferometer with sub-angstrom displacement resolution for electrostriction measurements," *Meas. Sci. Technol.* **14**, 766-772 (2003).

<sup>18</sup>H. E. Grecco and O. E. Mart Inez, "Calibration of subnanometer motion with picometer accuracy," *Appl. Opt.* **41**, 6646-6650 (2002).

<sup>19</sup>K. G. Libbrecht, E. D. Black, and C. M. Hirata, "A basic lock-in amplifier experiment for the undergraduate laboratory," *Am. J. Phys.* **71**, 1208-1213 (2003).

<sup>20</sup>R. Worlfson, "The lock-in amplifier—A student experiment," *Am. J. Phys.* **59**, 569-572 (1991).

<sup>21</sup>P. Nachman, P. M. Pellegrino, and A. C. Bernstein, "Mechanical resonance detected with a Michelson interferometer," *Am. J. Phys.* **65**, 441-443 (1997).

<sup>22</sup>See supplementary material at <http://dx.doi.org/10.1119/1.4901972> for a student lab manual.

<sup>23</sup>A commercial version of this interferometer is available at <<http://www.newtonianlabs.com>>.